3.4 Adjustment to an Obstacle in a Rotating Channel

When this text is revised again, it would be nice if the whole section could be shortened. Areas that might be made more concise include Section g.

There is a reference to Appendix (D??) describing a numerical code. This Appendix has not been written.

Need to scan the 3D figure from the 1983 JFM paper.

Although the process of Rossby adjustment provides valuable insight into the nature of transients in rotating channels, a further step is necessary to relate these transients to the establishment of hydraulically controlled states. The Long adjustment problem for nonrotating flow (Long, 1954 and 1970, Sections 1.6 and 1.7) provides a vehicle for doing so. In the original laboratory version of the experiment, an obstacle is towed at a fixed speed through a channel of shallow, resting fluid. Numerical versions of the experiment [e.g. Houghton and Kasahara (1968), Baines and Davies (1980)] place a fixed obstacle in the path of an initially steady, uniform flow, which is equivalent to the original set-up provided frictional effects are negligible. The outcome of the experiment for a single layer with a free surface depends on the Froude number $F_0 = v_0 / \sqrt{g d_0}$ based on the initial depth d_0 and velocity v_0 of the moving stream and on a nondimensional obstacle height h_m/d_0 (Figure 1.13). For a given value of F_0 the outcome depends largely on whether h_m/d_0 exceeds a critical height (given by curve BAE). Beyond this height the obstacle partially blocks the approaching flow through the generation of a bore that moves upstream. The steady flow left behind has reduced volume transport and is hydraulically critical (hydraulically controlled) at the sill of the obstacle. For sufficiently large h_m/d_0 (given by the curve BC) the flow is completely blocked. Other boundaries can be calculated such as the curve AD, which separates flow having hydraulic jumps on the downslope of the obstacle from those that do not. Regime diagrams such as Figure 1.13 and its generalizations in multi-layered flow are wonderful tools for developing knowledge and intuition about jumps, bores, upstream influence, hydraulic control, and hydraulics in general. They also give an indication of how high a topographic sill must be in order to establish hydraulic control. More sophisticated versions of such models might indicate how high the sills in the abyssal ocean must be in order to alter the meridional overturning cell.

Rotating versions of Long's experiment are quite difficult to carry out in the laboratory. Progress can and has been made using numerical models such as the one described in **Appendix D?? (this will be the section on a numerical code)**. If the potential vorticity of the flow is uniform, predictions of the critical obstacle height and of certain aspects of the final steady solution can be made using the semi-geostrophic theory developed in Sections 2.1-2.5. However, the extent to which features such as hydraulic

jumps can be predicted is limited by the lack of a shock-joining theory for rotating jumps and bores, a subject explored in later sections of this chapter. The following discussion is based largely on the work of Pratt, 1983b and Pratt, Helfrich and Chassignet, 2000.

a. Initial conditions.

In a rotating environment, the act of towing an obstacle along the channel at a fixed speed through an initially stationary fluid is no longer equivalent to introducing a stationary obstacle in a moving stream of the same speed. In the first case the free surface is horizontal; in the second it has a cross-stream, geostrophic tilt. We will consider the second version of the experiment since the upstream states seem more meaningful for ocean applications. The obstacle will therefore be introduced into a steady current that is varies with x but is uniform in y. This current will be required to have uniform potential vorticity f/D_∞. For scaling purposes, the local depth D will be considered equal to the potential depth D_∞; the nondimensional potential vorticity is therefore given by $q= D/D_\infty=1$. As was the case in the Rossby adjustment problem, the dimensionless decay scale of Kelvin waves across the channel will be unity. The choice of uniform (and nonzero) potential vorticity will naturally lead to comparisons with the Gill (1977) model for steady flow (Section 1.5).

If the potential vorticity remains at its initial value $q=1$ throughout the adjustment and if the along-channel variations remain weak, than the cross-section profiles of depth and velocity are given by expressions developed in Sections 2.2 and 2.3 for semigeostrophic flow. For example the profiles of d and v for non-separated flow are described by (2.2.3) and (2.2.4). The average $\overline{B}$ of the semigeostrophic Bernoulli functions $v^2/2+d+h$ on the two side walls is given by

$$\overline{B} = \tfrac{1}{2}[T^{-2}\hat{d}^2 + T^2(\overline{d}-1)^2] + \overline{d} + h \qquad (3.4.1)$$

where $T=tanh(w/2)$. The volume transport and Froude number are given by

$$Q = 2\overline{d}\hat{d}. \qquad (3.4.2)$$

and

$$F_d = \frac{\hat{d}}{\overline{d}^{1/2}T[1-T^2(1-\overline{d})]^{1/2}} \qquad (3.4.3)$$

For detached flow the equations governing steady flow can be obtained by replacing $\hat{d}$ by $\overline{d}$ and T by $T_e=tanh(w_e/2)$ in these expressions.

To maintain continuity with Long's original experiment, we continue to use the Froude number of the initial flow, defined by (3.4.3), and the dimensionless obstacle height h_m/D_∞, to characterize the initial conditions. However, the presence of rotation brings two additional parameters into play. One is the channel width w (the dimensional

channel width divided by $L_d=(gD_\infty)^{1/2}/f$), which determines the overall strength of rotation. A fourth parameter is Gill's ψ_i, which determines relative amounts of volume flux contained in the right- and left-wall boundary layers of the initial flow. As a starting point, we will fix ψ_i by requiring that the total volume flux of the initial flow be contained in the left-wall boundary layer. For this scenario to make sense, one should imagine that the channel broadens into a wide reservoir far upstream of where the initial value experiment is to be performed. There the separation of the flow into left- and right-wall boundary layers is clear. A flow fed entirely by the left hand boundary layer could have been set up as the result of a dam break experiment in which motion is triggered by a Kelvin wave propagating upstream along the left wall.

The procedure for specializing the initial conditions to give zero approach flow along the right wall of the hypothetical reservoir is based on conservation of energy along that wall. Since the flow along the reservoir's right wall is stagnant, the value of the Bernoulli function there is unity (dimensionally gD_∞), and thus

$$\frac{v_0{}^2(w/2)}{2}+d_0(w/2)=1,$$

where $(\,)_0$ signifies the initial value. If (2.2.5-2.2.8) are used to write this relation in terms of $\bar{d}$ and $\hat{d}$ the result may be expressed in the nondimensional form:

$$\frac{[(\hat{d}_0/T)-T(1-\bar{d}_0)]^2}{2}+\bar{d}_0+\hat{d}_0=1. \qquad (3.4.4)$$

To fix the initial conditions for given F_d and w the values of $\bar{d}_0$ and $\hat{d}_0$ must be computed. Once known, these two quantities completely determine the initial depth and velocity profiles through (2.2.3) and (2.2.4). Equation (3.4.4) provides one equation for $\bar{d}_0$ and $\hat{d}_0$ while (3.4.3) provides a second. If $\hat{d}_0$ is eliminated between these two relations the following equation for $\bar{d}_0$ is obtained:

$$\tfrac{1}{2}\{F_d\bar{d}_0^{1/2}[1-T^2(1-\bar{d}_0)]^{1/2}-T(1-\bar{d}_0)\}^2+\bar{d}_0+F_dT\bar{d}_0^{1/2}[1-T^2(1-\bar{d}_0)]^{1/2}=1. \qquad (3.4.5)$$

It may turn out that the initial flow is separated from the left wall of the channel, in which case the above calculation will give $\bar{d}_0 < \hat{d}_0$. In this situation, the parameter T in (3.4.5) must be replaced by the *variable* $T_{e0}=\tanh(w_{e0}/2)$, where w_{e0} is the initial width of the separated current. The initial condition is now specified by the value $\bar{d}_0$ (now equal to $\hat{d}_0$) and T_{e0}, and both are related by

$$\bar{d}_0=\frac{F_d^2(1-T_{eo}^2)}{T_{e0}^{-2}-F_d^2T_{eo}^2}, \qquad (3.4.6)$$

which follows from (3.4.3). Substitution of this relation into (3.4.5) results, after some rearrangement, in

$$\frac{(F_d^2-1)^2}{2}+(1-F_d^2T_{eo}^4)(2F_d^2-F_d^2T_{eo}^2-T_{eo}^{-2})=0 \qquad (3.4.7)$$

The procedure is to first solve (3.4.7) for T_{e0} and then calculate the corresponding value of $\overline{d}_0$ from (3.4.6).

One consequence of the assumption that the volume flux in the initial flow is fed from the reservoir's left-hand boundary layer is that separated initial flow cannot be subcritical. The proof is the subject of Exercise 1.

b. The critical obstacle height.

It is anticipated that only values of h_m greater than some critical value h_c will lead to upstream influence: permanent alteration of the upstream flow. In Long's experiment the prediction of h_c follows from the consideration of a *steady* flow that passes over the obstacle and has the same volume flux Q and Bernoulli constant B as the initial state under consideration. There is a maximum h_m for which the upstream energy B is sufficient (at the given Q) to allow the fluid to surmount the crest. As shown in Chapter 1, hydraulically criticality occurs at the sill when the upstream flow has the minimum B required to surmount the obstacle. If h_m exceeds the maximum allowable value, the values of B and/or Q must be altered in order to allow the flow to continue and this implies generation of an upstream disturbance that alters the values of Q and B. Thus, the predicted h_c for given initial Q and B is that height for which these Q and B would, in a steady state, produce critical sill flow. An application of the same principles (with the upstream state now specified by F_d and w) results in a prediction of h_c in the rotating case.

For given initial values F_d and w, a unique initial flow with $\overline{d}=\overline{d}_0$ and $\hat{d}=\hat{d}_0$ is determined by the procedure laid out in *(a)*. Consider a hypothetical steady flow with upstream values $\overline{d}_0$ and $\hat{d}_0$ that becomes critical ($\overline{d}=\overline{d}_c$ and $\hat{d}=\hat{d}_c$) at the crest ($h=h_c$) of the obstacle. Conservation of mass (3.4.2) requires that

$$\hat{d}_0\overline{d}_0=\hat{d}_c\overline{d}_c \qquad (3.4.8)$$

Together with the condition of criticality at the sill (F_d=1 in 3.4.3), (3.4.8) implies that

$$\overline{d}_c^{\,4}+\frac{1-T^2}{T^2}\overline{d}_c^{\,3}-T^{-4}(\hat{d}_0\overline{d}_0)^2=0 \qquad (3.4.9).$$

This equation determines $\overline{d}_c$ given the upstream/initial quantities $\hat{d}_0$ and $\overline{d}_0$. The value of $\hat{d}_c$ then follows from (3.4.2). Once $\overline{d}_c$ and $\hat{d}_c$ have been found it must be determined whether or not the flow at the sill is separated. If $\overline{d}_c \geq \hat{d}_c$ the flow is not separated and one may proceed to the next step, as described below. If $\overline{d}_c < \hat{d}_c$ the flow at the sill is separated from the left wall, and a revised procedure must be used (see Exercise 2). In either case the properties of the critical flow at the sill are known.

The critical sill height h_c can now be computed by equating the energy at the sill with that upstream. Employing the Bernoulli equation (3.4.1) with the computed values of $\hat{d}_c$ and $\overline{d}_c$ leads, in the case of non-separated flow, to

$$h_m = 1 - \hat{d}_0\overline{d}_0 - \tfrac{1}{2}[T^2(\overline{d}_c - 1)^2 + (\hat{d}_c / T)^2 + 2\overline{d}_c] \qquad (3.4.10a)$$

When the sill flow is separated, this relation is replaced by

$$h_m = 1 - \hat{d}_0\overline{d}_0 - \tfrac{1}{2}\{T_{ec}^2[(\hat{d}_0\overline{d}_0)^{1/2} - 1]^2 + \frac{\hat{d}_0\overline{d}_0}{T_{ec}^2} + 2(\hat{d}_0\overline{d}_0)^{1/2}\} \qquad (3.4.10b)$$

with

$$T_{ec}^2 = \left(\hat{d}_0\overline{d}_0\right)^{1/2} / \left[1 - \left(\hat{d}_0\overline{d}_0\right)^{1/2}\right]$$

(see Exercise 2).

The relationship between h_m and F_d is shown for a case of weak rotation (w=0.5). by the curve CAE in Figure 3.4.1. The curve is composed of a number of segments indicating various states of separation. To the left of CAE, there is no predicted upstream influence and the final flow upstream and downstream of the obstacle is identical to the initial flow. The final flow is altered directly over the obstacle but it does not become critical. To the right of CAE the predicted final upstream and downstream states have been altered by (unknown) transients. The predicted flow over the obstacle is critical at the sill and supercritical in the lee, possibly with some form of hydraulic jump. On CAE, the predicted flow is critical at the obstacle crest but the upstream flow is unaltered. Along the solid segment BA′, both the initial flow and the predicted sill flow are non-separated. Along BC, which lies at the extreme lower right of the diagram, and is enlarged in an inset, the initial flow is attached but the predicted critical sill flow is separated. The predicted final flow thus separates from the left wall at some point slightly upstream of the sill. To the immediate left of BC the upstream flow is attached and subcritical and the predicted flow over the obstacle is also subcritical but detached at the sill. In the upper portion of the diagram corresponding to supercritical initial flow (F_d>1) lies a segment A′E spanning a range of Froude numbers for which the initial flow is separated. Along sub-segment A′H the predicted sill flow is critical and attached while

along HE the sill flow is critical and separated. To the immediate left of A′H lies a wedge-shaped region A′HG in which the predicted final flow is supercritical everywhere, separated upstream and downstream of the obstacle, and attached near the sill. To the left of HE the predicted final flow is supercritical and separated everywhere.

An idea of the influence of rotation on the critical obstacle height can be gained by inspection of Figure 3.4.2, which shows the critical height curve CAE from the above weak rotation case (w=0.5) plotted along with the w=2 relation. For subcritical initial conditions rotation reduces the critical obstacle height whereas the reverse is true when the initial flow is supercritical. Note that the two curves merge when F_d is sufficiently large. Here the initial flow and the predicted sill flow are separated, implying that w is no longer a factor in determining h_m.

Along segment BC of Figure 3.4.1 the initial flow is attached and the predicted critical sill flow separated, as shown in the lower right inset. Reduction of the sill height with fixed F_d eventually results in reattachment of the flow at the sill, resulting in a state that is completely attached and subcritical (i.e. lower middle inset). The value of h_m at which reattachment occurs (i.e. $d_s(-w/2)=0$ and $w=w_e$) will be denoted h_s. The value h_s of the sill height at which reattachment occurs can be found by replacing the critical condition in the steps leading to (3.4.10a) by the condition of marginal separation ($\overline{d} = \hat{d}$ and $T_e=T$) at the sill. This procedure results in

$$h_s = \tfrac{1}{2}T^2[(\overline{d}_0 - 1)^2 - (\overline{d}_s - 1)^2] + \frac{\hat{d}_0^2 - \overline{d}_s^2}{2T^2} + \overline{d}_0 - \overline{d}_s \qquad (3.4.11a)$$

where $\overline{d}_s = \hat{d}_s = (\overline{d}_0\hat{d}_0)^{1/2}$. The curve of h_s vs. F_d is given by DB in the inset at the right of Figure 3.4.1. To the left of this curve the predicted flow is subcritical and attached everywhere. In the region DBC, the flow is separated at the sill, attached upstream and downstream of the obstacle, and subcritical everywhere.

Similarly, there exists a range of supercritical initial conditions for which the predicted final states are supercritical everywhere, separated upstream and downstream of the sill, and marginally separated at the sill. As before, the obstacle height h_s for such solutions is smaller than the corresponding critical height and can be calculated by replacing the critical condition by the condition of marginal separation, this time in the steps leading to (3.4.10b). The procedure yields

$$h_s = \tfrac{1}{2}(T_{e0}^{2^-}T^2)(\overline{d}_0 - 1)^2 + \frac{\hat{d}_0^2 - \overline{d}_s^2}{2T^2} + \tfrac{1}{2}\hat{d}_0^2(T_{e0}^{-2} - T^{-2}) \qquad (3.4.11b)$$

and corresponding curve is labeled GH in Figure 3.4.1. The region GHA′ contains flows that are supercritical everywhere, separated upstream and downstream of the sill, and attached at the sill, as shown by the inset. To the left of GE the predicted final flows are supercritical and separated everywhere.

c. Overview of the temporal evolution.

Numerical solutions based on the full shallow-water equations show some similarities and important differences with what the semigeostrophic theory predicts. The runs are started at $t = 0$ with the flow specified in terms of F_d and w as described above. A Gaussian obstacle

$$h = h_o(t)\exp(-y^2/4)$$

is then quickly grown into the flow by increasing $h_0(t)$ linearly from zero to h_m.

The numerical results are summarized in Figures 3.4.3-24 for channel widths w = 0.5, 2, and 4, respectively. The regime curves from the semigeostrophic theory are shown along with the locations of numerical runs. The circles indicate solutions exhibiting a lack of permanent alteration of the original flow and the squares show cases exhibiting permanent upstream influence. The numerical results show versions of most of the features, including bores and jumps, that arise in Long's original experiments. They also reveal some features which are remarkable and unexpected. Since it is not possible to discuss each numerical run in detail, the reader is referred to the thumbnail insets in the three figures showing characteristic behavior found in different regions of the parameter space. These insets contain contours of the free surface height, $d(x,y,t)+h(y)$, at later stages of the flow development. They illustrate the final steady flows over the topography and, in some cases, the structure of transient features. The gray shaded regions in some of the insets indicate areas of the channel that are 'dry'.

The occurrence of upstream influence is indicated by asymmetry in the along channel direction of the final steady flow over the topography and by a reduction in the transport at the sill crest compared to the initial transport. For subcritical initial flow ($F_d < 1$) the numerically determined transition to upstream influence agrees reasonably well with the semigeostrophic theory for $w = 0.5$ and 2 (Figures 3.4.3 and 3.4.4). For $w = 4$ and small F_d (Figure 3.4.5) the numerical results indicate upstream influence for smaller values of h_m than predicted by the theory. The agreement extends to $F_d > 1$ for the narrow channel ($w = 0.5$, Figure 3.4.3). For $w = 2$ and 4 (Figures 3.4.4 and 3.4.5) the transition to upstream influence occurs at moderately larger values of h_m than predicted by the theory, though the general behavior of the transition as a function of F_d follows the theory for the few values of $F_d > 1$ that have been investigated.

The disagreement between the numerically determined transitions and the semigeostrophic theory with increasing channel width is not surprising. In narrow channels the confinement provided by the wall suppresses cross-channel accelerations and thus the along-channel flow should remains nearly geostrophic. For wider channels this effect is weakened and large cross-channel accelerations occur over the sill in the initial adjustment phase leading to departure from the semigeostrophic prediction. Non-conservation of potential vorticity could also affect the value of the critical height. The numerical model includes weak lateral viscosity and thus does not conserve potential

vorticity following fluid parcels exactly as the analytical model does. As we shall see later, fluid parcels that pass through shocks can suffer a change in potential vorticity due to dissipative processes therein.

d. The case w=0.5 (weak rotation).

We begin the discussion of the flow evolution by examining the case $w = 0.5$, as summarized in Figure 3.4.3. Despite the narrowness of this channel, rotation can be quite important. First consider some examples for which there is no predicted upstream influence ($h_m<h_c$) as illustrated by the insets on the left-hand side of Figure 3.4.3. Subcritical conditions give rise to an acceleration of the flow accompanied by a deflection of streamlines over the obstacle towards the right wall(e.g. F_d=0.5, h_m=0.1). The opposite occurs for supercritical initial conditions, as exemplified by the case (F_d =1.5, h_m=0.04). If F_d is large enough the initial supercritical flow is separated and the corresponding final steady states may either be completely separated (F_d=2.5, h_m=0.1) or separated away from but attached near the sill (F_d =2.5, h_m = 0.3). This last case is shown in greater detail in Figure 3.4.6. At t=10 the disturbance generated by the introduction of the topography is evident immediately downstream of the sill. It consists of two waves that propagate downstream. The first is the faster Kelvin wave, centered at about y=15, and the second is the slower frontal wave (Section 2.3), centered at about y = 8. By t =20 the Kelvin wave has propagated out of the domain and the frontal wave (near y=17) has steepened, nearly to the point where the stream width w_e is discontinuous.

As noted above, upstream influence for the case w=0.5 generally occurs where predicted ($h_m>h_c$). When the initial flow is attached, the disturbance that alters the upstream state takes the form of a 'Kelvin-wave' bore. Figure 3.4.7 shows an example of this process for F_d = 0.5, h_m= 0.2. At t = 10 both upstream and downstream propagating Kelvin waves are evident on each side of the topography. The characteristic trapping of the Kelvin waves to the side walls is weakly apparent in this narrow channel. By t =30 the downstream wave has left the domain, the upstream wave has steepened into a bore, and a hydraulic jump has formed on the downstream side of the obstacle. The jump remains over the downstream face of the obstacle in the final steady flow (t= 50). The Froude number (3.4.3) calculated from the numerical solution at t = 30 indicates a transition from subcritical to supercritical flow over the sill and a return to subcritical flow across the downstream jump (bottom panel of Figure 3.4.7). Also note how F_d decreases across the upstream bore. Generally speaking, the solution is similar to the nonrotating case. The most apparent sign of rotation is the deflection towards the right wall of the supercritical flow in the lee of the obstacle.

As in the nonrotating case, low values of the initial F_d favor stationary hydraulic jumps whereas higher values tend to cause the jumps to move downstream. The latter is illustrated by the inset in Figure 3.4.3 for F_d=1 and h_m= 0.2, where the former hydraulic jump is shown as a discontinuity moving away from the topography in the downstream direction. With no rotation the boundary in the (h_m, F_d) plane separating regimes with and without jumps can be constructed analytically using shock joining theory. This

boundary is given by the curve AD in Figure 1.13. A similar calculation is hindered in the rotating case due to the unavailability of a satisfactory shock joining theory.

There are also a number of instances where the supercritical flow downstream of the sill separates from the left wall, a behavior that has important ramifications for downstream disturbances. A good example is the case $F_d = 1.5$ and h_m=0.5 (Figure 3.4.8). At $t = 10$ the downstream-propagating Kelvin wave and upstream propagating bore are evident. The flow approaching the sill is accelerated and veers toward the right wall downstream of the crest leaving a small patch of dry channel near the left wall. The transition back to attached flow near $y = 7$ occurs as an abrupt expansion (located near y=16 at t=30). This transition is swept down the channel enlarging the dry region ($t = 30$) and ultimately leaving behind a detached supercritical flow in the lee of the topography ($t = 50$). The characteristic speed c_- has been calculated from (2.15) at points slightly upstream of and slightly downstream of the abrupt transition. On the upstream side, where the flow is separated and frontal wave dynamics apply, c_- is positive and greater than on the downstream side, where the flow is attached and Kelvin wave dynamics apply. Thus, linear disturbances generated just upstream of the transition overtake those generated just downstream, indicating that the transition is indeed a shock.

Flow separation in the lee of the obstacle is also observed for subcritical initial conditions and large values of h_m. In cases where hydraulic jumps occur, the usual abrupt change in depth is replaced by an abrupt change in the width of the stream. The jump is much like the transition in Figure 3.4.8, but with the feature stationary in the lee of the topography. An example (for F_d= 0.5, h_m = 0.8, Figure 3.4.9a) has a dry patch of bottom (shaded region in $1<y<2.3$) immediately downstream of the sill. This separated region terminates in a sudden expansion and reattachment of the flow. Downstream of the jump is a zone of cyclonic recirculation. A plot of F_d along with the left-wall depth (Figure 3.4.9b) shows that the transition from detached ($d(-w/2,y)$ =0) to attached flow near y=2.3 coincides with a supercritical to subcritical transition. This type of expansion is called a *transverse hydraulic jump* and its dynamics will discussed later in this chapter.

When the initial flow is separated, upstream influence occurs in an unexpected manner. The leading portion of the upstream moving disturbance is a rarefying intrusion attached to the left wall as illustrated in the inset in Figure 3.4.3 for F_d=2.5 and h_m=0.5. In this example the intrusion is followed by a surge that leaves behind attached flow upstream of the sill. The surge results in a rapid increase in depth, however the front is smooth and behaves like a rarefaction rather than a shock. We will return to this interesting situation below.

The foregoing examples show that rotation can lead to remarkable effects even when w is moderately small. These effects occur where high velocities are present, either due to supercritical initial conditions or because high velocities are induced in the lee of large obstacles. The high velocities lead to strong tilts in the free surface, sometimes resulting in separation of the flow. The Rossby radius of deformation based on the *local* depth becomes small in such cases and it is no surprise that inherently rotational features such as the transverse hydraulic jump arise under these conditions.

A final remark about the case w=0.5 is that Pratt et al (2000) were not able to verify the subcritical flow which briefly detaches over the sill (predicted in region DBC in Figure 3.4.1). Nor were they able to do so for other values of w. The hydraulically controlled flows to the immediate right of BC have attached flow at the sill, despite the prediction to the contrary. In fact, no instance was found for any w in which the sill flow is simultaneously separated and hydraulically controlled.

e. Cases w=2 and w=4 (strong rotation).

The regime diagrams for the cases *w=2 and w=4* (Figures 3.4.4 and 3.4.5) show that separation of the initial flow now occurs for nearly all F_d>1, as indicated by dashing of the critical obstacle height curve. A region analogous to A′HG of Figure 3.4.1 exists for each case but is indistinguishably thin; its upper boundary is indicated by a horizontal bar in each figure. This bar marks that value of F_d above which the predicted critical sill flow is separated.

Strong rotation has consequences for the structure of the transients that occur when the supercritical flow remains attached, and this is demonstrated by the case F_d=0.5, h_m=0.2 and w=2 (Figure 3.4.10). Upstream influence is established as before by a 'Kelvin wave' bore and a stationary jump forms downstream. In contrast to the case w=0.5 (c.f., Figure 3.4.7) neither the bore nor the jump extend across the channel, but rather are strongly trapped to the left wall. The downstream jump has a lateral scale of only about 0.5, or half of a deformation radius. Downstream of the jump a region of cyclonic recirculation is generated. This region appears to expand in the downstream direction indefinitely. The structure of the bore and jump are evident in the topography of the free surface (Figure 3.4.11). When h_m is increased well beyond the critical value the lee flow tends to detach, then reattach over the topography to form a transverse jump, as discussed above.

For F_d>1 the initial flow is separated for all Froude numbers save those close to unity. Upstream influence for these separated cases occurs in an unexpected manner, as demonstrated by the case F_d = 1.5, h_m= 0.4 and w=2 (Figure 3.4.12). Although the initial flow is separated, the predicted critical flow at the sill is attached. Upstream influence occurs as the result of a bifurcation of the initial current over the topography (t=20). A portion of the incident flow is diverted back towards negative y, forming a separated, rarefying intrusion along the left wall, while the rest continues over the topography (t=40). The original current and upstream intrusion are narrow and do not contact each other. The final steady state upstream of the topography consists of two opposite, separated currents (t=50). Remarkably, there is no upstream influence in the original current. However, the net flux towards the sill is reduced by the diversion of fluid into the left-wall intrusion.

Numerical calculations have also been carried out using F_d values sufficiently large that the predicted critical sill flow is separated. Such values lie above the horizontal bars in Figures 3.4.4 and 3.4.5. Significantly, these settings also result in left wall

intrusions of the type just discussed and in attached flow at the sill. In no cases did they observe sill flows that are critical and separated at the sill.

In the case of the widest channel considered (w=4) the flow responds much as in the w=2 case. One qualitative difference, evident for flows with F_d<0.5, is the appearance of an anticyclonic recirculation cell over the sill. This feature occurs regardless of the presence of upstream influence, as illustrated by the two insets in Figure 3.4.5 for F_d = 0.1 and h_m=0.2 and 0.45. In the run with F_d=0.1, h_m=0.2 the velocity on the right wall at the sill crest $v(w/2,0) < 0$. The recirculation cell occupies about three-quarters of the channel width, forcing the fluid that crosses the sill and continues downstream to do so in a narrow band adjacent to the left wall. The along-channel extent of the recirculation is comparable to the length of the topography. The existence of a counterflow at the sill is in violation of theorem (Exercise 3 of Section 2.5) governing uniform-potential vorticity, semigeostrophic flow.

f. The lack of hydraulic control of separated flows.

Many models of steady, hydraulically-driven flow in rotating channels, including the pioneering studies of Whitehead et al. 1974 and Gill 1977 (Sections 2.4 and 2.5) describe solutions that are hydraulically critical and separated at the controlling sill or narrows[1]. Shen (1981) and Pratt (1987) attempted to reproduce such flows in the laboratory and were unsuccessful. Whitehead et al. (1974) claimed to have achieved separated and hydraulically controlled flow in the laboratory, but their 'sill' was actually a finite-length segment of rectangular channel over which the bottom elevation and width is constant. Although the flow is separated in the downstream portion of this segment, it is not so at the upstream portion. The exact section of critical flow and its state of separation are unknown.

The present numerical simulations also fail to produce hydraulically controlled flows that are separated at the sill section. Such states might have been expected as a result of runs such as F_d = 1.5 and h_m=0.4 of Figure 3.4.5, in which the initial flow is separated and the predicted sill flow is also separated. However, the obstacle causes deflection of the approaching flow to the left wall resulting in the formation of an intrusion as in Figure (3.4.12). Over the sill itself, the flow becomes attached. Other cases where the sill flow is predicted to be separated and critical correspond to very subcritical, attached initial flows and large h_m (as in the region just to the right of curve BC in Figure 3.4.1). Although the numerical experiments confirm that the flow is controlled, it remains attached at the sill.

These findings seem to suggest the presence of an instability that acts when a separated flow is critical or subcritical. However, Paldor (1983) has shown that separated currents of the type under discussion are stable, at least in the limit of zero potential vorticity, provided that the fluid depth along the right wall remains non-zero. So there

[1] Examples can be found in Gill's (1977) Figures 6 and 7, and 9d.

does not yet appear to be a clear connection between inviscid instability and the lack of separated critical flow in the numerical experiments. A second cause could be the apparent difficulty for bores in separated flows to propagate upstream. This aspect is illustrated in Figure 3.4.12 where at t=10 the separated initial flow collides with the obstacle, resulting in a widening of the current. One might have expected an upstream disturbance to be generated within the separated approach flow. Such a disturbance would establish a hydraulically controlled flow that remains separated from the left wall. However, the figures shows that an upstream disturbance is not generated until contact with the left wall is made.

In general, the lack of hydraulic control of separated flows, both in numerical and laboratory experiments, remains a mystery.

g. Breakdown of semigeostrophic theory.

Large channel widths permit the formation of larger cross-channel velocities, leading to the departures from semigeostrophic behavior. One way to document such departures is through the semigeostrophic Froude number. Figure 3.4.13*c* contains a longitudinal plot (solid line) of the constant potential vorticity, semigeostrophic Froude (3.4.3) for the flow shown frame *a*. Surprisingly F_d never exceeds unity, reaching a maximum value $\cong$0.95 just upstream of the hydraulic jump. The value at the sill is considerably lower. The fact that this example clearly exhibits upstream influence, and that something like a hydraulic jump exists, suggests F_d should equal 1 at the sill and exceed 1 immediately downstream. Apparently (3.4.3) is no longer a reliable definition of the Froude number. As shown in frame *c*, significant cross-channel velocities exist near and slightly downstream of the sill, suggesting that the failure of (3.4.3) may be due to a loss of semigeostrophy. This failure could also be due to potential vorticity non-uniformity that might have developed in the flow field.

In order to test the last hypothesis, consider Stern's generalized critical condition (Section 2.9)

$$\int_{-w/2}^{w/2} (v^2 d)^{-1} (1 - \frac{v^2}{d}) dx = 0 , \qquad (3.4.12)$$

valid only when d remains positive and v remains single signed in $-w/2 \geq y \geq w/2$. This expression suggests a generalized Froude number

$$F_S^{\,2} = \frac{\int_{-w/2}^{w/2} d^{-2} dx}{\int_{-w/2}^{w/2} (v^2 d)^{-1} dx} , \qquad (3.4.13)$$

which equals unity when the flow is hydraulically critical. Although F_S does exceed unity on the downstream face of the obstacle (dashed curve in Figure 3.4.13c), its value

(≅0.4) at the sill is even lower than the value of F_d there. This behavior suggests that the breakdown in our measure of the Froude number is due to the failure of the semigeostrophic approximation. This conclusion is supported by the behavior of the Froude number in a flow regime with the same obstacle height but a narrower channel (*w=0.5,* Figure 3.4.8d), where F_d reaches and exceeds unity in the expected places.

In addition to failure the of (3.4.13) to measure the true criticality of the flow, there are other indications of breakdown of the semigeostrophic approximation. The value of the critical obstacle height h_c predicted by semigeostrophic theory agrees well with the observed values for the narrowest channel (w=0.5). As w increases the agreement grows worse; the predicted h_c overestimates the actual h_c for subcritical initial flows and underestimates it for supercritical initial flows. This trend is probably a result of the fact that large cross-channel velocities are allowed to develop once the channel width exceeds a deformation radius. Despite these differences the general shape of the curve of h_c as a function of F_d remains as predicted.

More striking breakdowns in the semigeostrophic approximation occur within individual features. Perhaps the most dramatic is the grounding or separation of the flow ($d \rightarrow 0$) in the interior of the stream, as occurs at the bifurcation of the upstream flow (t=20,40, and 80 in Figure 3.4.12 near y=-2.5) and at the detaching eddy (near y=14 and t=40 of the same figure). Such behavior is clearly in violation of Gill's (1977) theorem proscribing the vanishing of d at a point where $\partial^2 d / \partial x^2 > 0$ in any semigeostrophic flow (see Section 2.5). Not surprisingly, semigeostrophic theory also fails in the vicinity of jumps, bores and other transients exhibiting rapid transitions is the y-direction. It is not necessary that w be large for such violations to occur, as evidenced the presence of transverse jumps and bores when w=0.5 (Figure 3.4.3).

f. Upstream recirculations.

Although semigeostrophic theory admits solutions with closed recirculations, the location of the latter may be restricted by the assumed potential vorticity distribution. In Gill's (1977) uniform potential vorticity model, for example, it can be shown that the flow at any critical section must be unidirectional. Recirculations must therefore occur away from control sections. The laboratory simulations discussed in Section 2.6 contain recirculations, but in all cases the counterflow exists upstream of the sill crest. The potential vorticity distribution in these experiments is unknown. On the other hand, Section 2.9 makes it clear that flows with non-uniform potential vorticity may contain counterflow at a control section. The present numerical experiments contain examples in which recirculating fluid exists at the sill (Figure 3.4.14a). Inspection of the potential vorticity distribution across the sill confirms that it is non-uniform (Figure 3.4.14b). The boundaries of the recirculation (corresponding to ψ=0) occur at the right wall x=2 and at x≅-1 in the cross section taken at the sill. Within these boundaries q is roughly constant, in agreement with conditions conjectured by Borenäs and Whitehead (1998). To the left of the recirculation the potential vorticity is much higher.

h. Concluding remarks.

A review of the regime diagrams (Figures 3.4.3-3.4.5) suggests that most of the examples of hydraulically controlled flow can be placed in two broad classes. The first includes flows that remain attached to the left wall at each y. The time-dependent adjustment leading to the establishment of a controlled flow in this regime is similar to what takes place in Long's experiments, although the transients and the hydraulic jumps become trapped to the sidewalls. Energy dissipation due to jumps and upstream bores may be strongly localized near the left wall. One might collectively refer to these examples as the Kelvin-wave regime and note that it generally occurs for small-to-moderate F_d, h_m, and w. The second category includes flows that are separated from the left wall over some y. Significantly, the sill flow in all such cases remains attached. Further, all upstream disturbances and hydraulic jumps with separated upstream flow have attached downstream end states. Both Kelvin-wave and frontal-wave dynamics are important in these examples, which might collectively be referred to as a 'hybrid' regime. It is favored by large h_m, large F_d, and/or large w.

In no case is it possible to remove the left wall from the problem and still be able to realize a hydraulically controlled flow. Even when the initial flow is separated and w is large, the critical sill flow becomes attached to the left wall. In addition, upstream influence for large w is transmitted in the form of an intrusion that travels along the left wall. These results imply that a 'coastal' version of the current, set up by moving the left wall to infinity, cannot be hydraulically controlled nor have a stationary hydraulic jump. One caveat should be mentioned: by restricting the initial conditions so as to require zero volume transport in the left-hand boundary (Section 3.1) all separated initial flows are supercritical. There is another family of separated but subcritical initial flows that could conceivably be subject to upstream influence without the aid of the left wall. This path has not been explored.

For some of the interesting features found in the simulations, no concrete oceanographic observations have been reported at the time of this writing. Such features include the Kelvin-wave hydraulic jump (Figure 3.4.10), the transverse hydraulic jump (Figure 3.4.9), and the bifurcation of the flow approaching the sill with resulting leakage back into the upstream part of the channel (Figure 3.4.12).

Exercises

1) It has been assumed that the initial flow is fed entirely by a left-wall boundary layer. Show that such a flow, when separated, cannot be subcritical.

2) *Calculation of the critical obstacle height for separated sill flow.* Show that h_c is given by (3.4.10b) when the sill flow is separted ($\overline{d}_c < \hat{d}_c$). Hint: by using $\overline{d}_c = \hat{d}_c = (\hat{d}_0 \overline{d}_0)^{1/2}$ and $T = T_{ec} = \tanh(w_{ec}/2)$, first show that (3.4.9) yields

$$T_{ec}^2 = \frac{\left(\hat{d}_0 \bar{d}_0\right)^{1/2}}{1 - \left(\hat{d}_0 \bar{d}_0\right)^{1/2}}$$

then combine this relation with the Bernoulli equation.

3) Following the guidelines set down in the text, verify the relations 3.4.11a,b governing the curves DB and GH in Figure 3.4.1.

Figure Captions

Figure 3.4.1. Regime diagram showing the predicted response in terms of the initial Froude number F_d and the obstacle height h_m, all for a channel of width $w = 0.5$. The curve CAE gives the critical obstacle height, with different segments indicating different states of flow separation. The curves DB and GH indicate various states of flow separation for completely subcritical or supercritical flows. See the text for more details. (from Pratt et al. 2000)

Figure 3.4.2. Curves of critical obstacle height $h_m = h_c$ as a function of F_d for $w = 0.5$ and w=2. (from Pratt et al. 2000)

Figure 3.4.3. Summary of the numerical results for $w = 0.5$. The topography is given by The regime curves from the semigeostrophic theory are shown along with the locations of numerical runs. The circles indicate no permanent alteration of the original flow and the squares show cases of permanent upstream influence. Also shown are inset examples of the numerical results. The insets show contours of the free surface height ($d(x,y,t) + h(y)$). The shaded regions indicate those portions of the channel that are "dry" (defined by $d < 0.001$). The dashed lines are the 1, 0.5 and 0.001 times h_m contours of the bottom topography. The numerical model uses a uniform cell-centered grid with spacing in the along channel direction of $\Delta y = 0.05$. The cross-channel grid spacing and time steps range from ($\Delta x = 0.025$ and Δt=0.01) at $w = 0.5$ to ($\Delta x = 0.05$ and Δt=0.02) at $w = 2$ and 4. (from Pratt et al. 2000)

Figure 3.4.4. Same as Figure 3.4.3 except $w = 2$. Dashing of the critical obstacle height curve indicates those values of F_d for which the initial flow is separated. The thick horizontal bar overlaid on the critical obstacle height curve indicates the value of F_d above which the predicted critical sill flow is separated from the left wall. (from Pratt et al. 2000)

Figure 3.4.5. Same as Figure 3.4.3 except $w = 4$. (from Pratt et al. 2000)

Figure 3.4.6. Numerical results for F_d=2.5, h_m=0.3 and w=0.5. The panels show contours of the free surface height ($d(x,y,t) + h(y)$) at the times indicated. The shaded regions indicate those portions of the channel that are "dry" (defined by $d < 0.001$). The dashed lines are the 1, 0.5 and 0.001 times h_m contours of the bottom topography. (from Pratt et al. 2000)

Figure 3.4.7. Same as Figure 3.4.6, except F_d=0.5, h_m=0.2 and w=0.5. The bottom panel shows F_d as a function of y at t=30. (from Pratt et al. 2000)

Figure 3.4.8. Same as Figure 3.4.6, except F_d=1.5, h_m=0.5 and w=0.5. (from Pratt et al. 2000)

Figure 3.4.9. (a) Surface elevation contours for the steady flow that arises in the case F_d=0.5, h_m=0.8 and w=0.5. A transverse hydraulic jump lies at y≅2.3. (b) Plot of F_d (solid line) and $d(-w/2,y)$ (dashed line) for the flow in (a). The transition from supercritical to subcritical flow near y =2.3 coincides with the lateral expansion and reattachment of the flow to the left wall. (from Pratt et al. 2000)

Figure 3.4.10. Same as Figure 3.4.6, except F_d=0.5, h_m=0.2 and w=2. (from Pratt et al. 2000)

Figure 3.4.11 The top three frames show the free surface of the adjusting flow for the case F_d=0.41, h_m=.35 and w=1.1. The bottom frame shows the bottom topography and the flow is from right to left. (From Pratt. 1983b).

Figure 3.4.12. Same as Figure 3.4.6, except F_d= 1.5, h_m= 0.4 and w = 2. (from Pratt et al. 2000)

Figure 3.4.13. Details of the super- to subcritical transitions for the flow shown in the inset of Figure 3.4.4 with F_d=0.5 and h_m=0.5. (a) Contours of the free surface elevation $d+h$. (b) Contours of the dissipation $\mu\mathbf{u}\cdot(\nabla\cdot(d\nabla\mathbf{u}))$. The contour interval is 1.25×10^{-2}. (c) Contours of the transport streamfunction (dashed lines) overlaid with the dissipation contours from above. (d) The Froude number F_d based on Equation 3.4.3 (solid line) and F_S based on Equation 3.4.13 (dashed line). The definition of F_S is invalid downstream of the jump (at y≅1) due to velocity reversals. (from Pratt et al. 2000)

Figure 3.4.14. (a) Surface height contours for the case (w=4, F_d=0.1, and h_c= 0.45) in which a recirculation exists over the sill. (b) Potential vorticity and streamfunction profiles at the sill (y=0). (from Pratt et al. 2000)

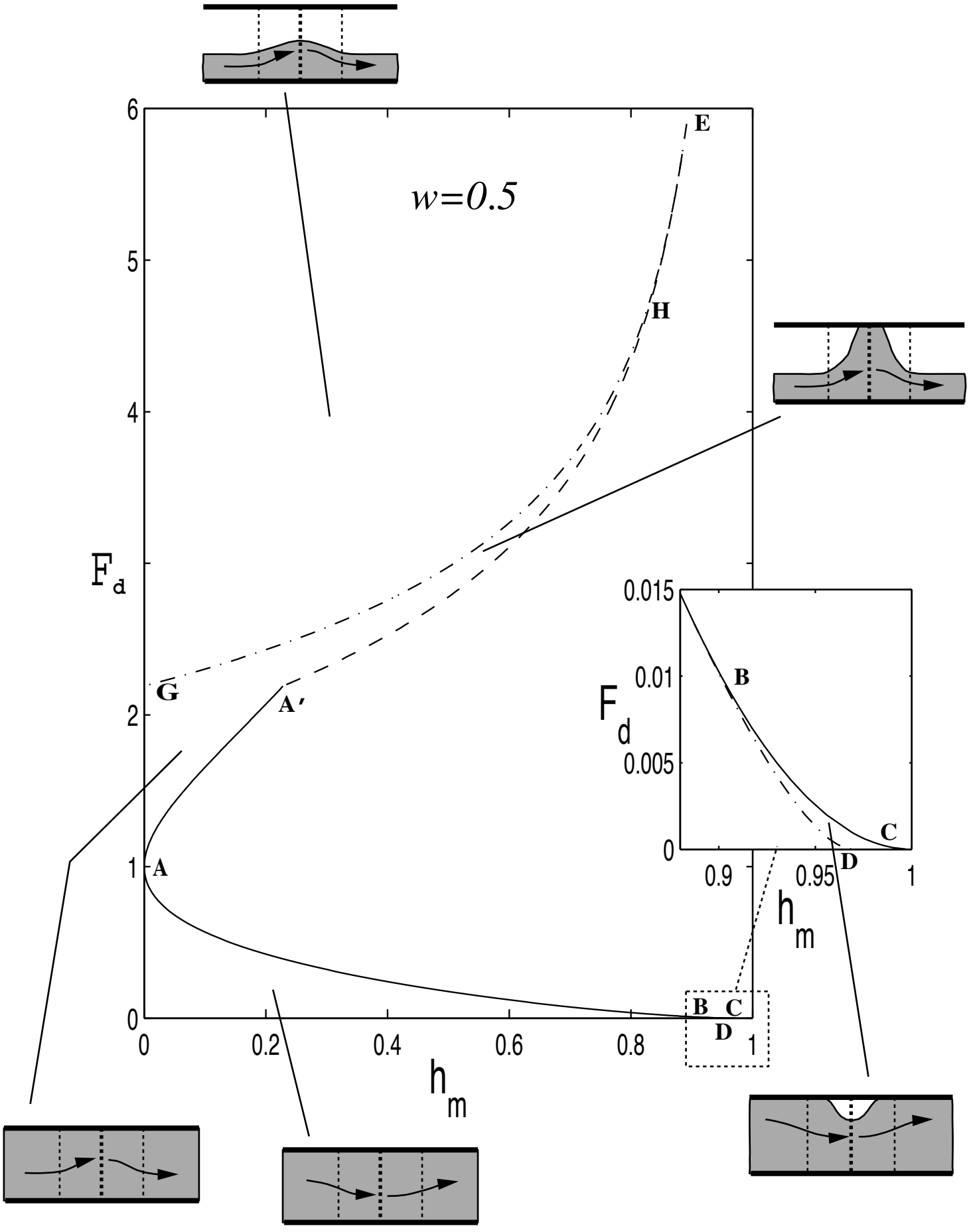

Figure 3.4.1

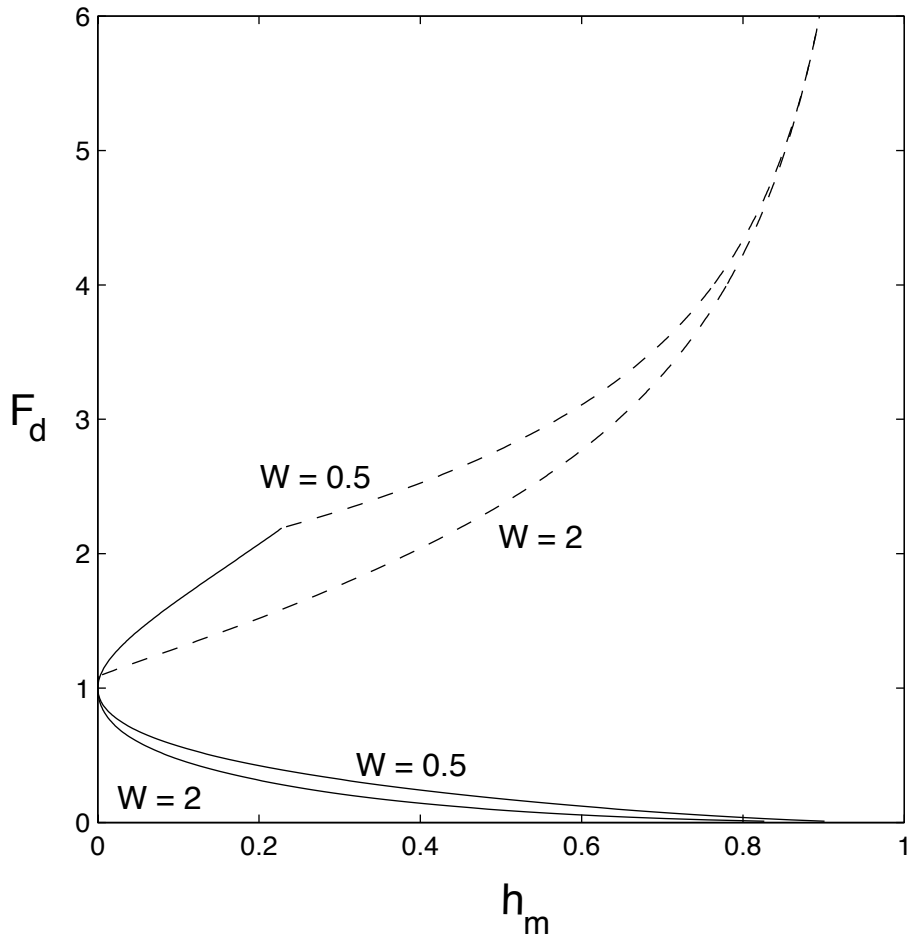

Fig. 3.4.2

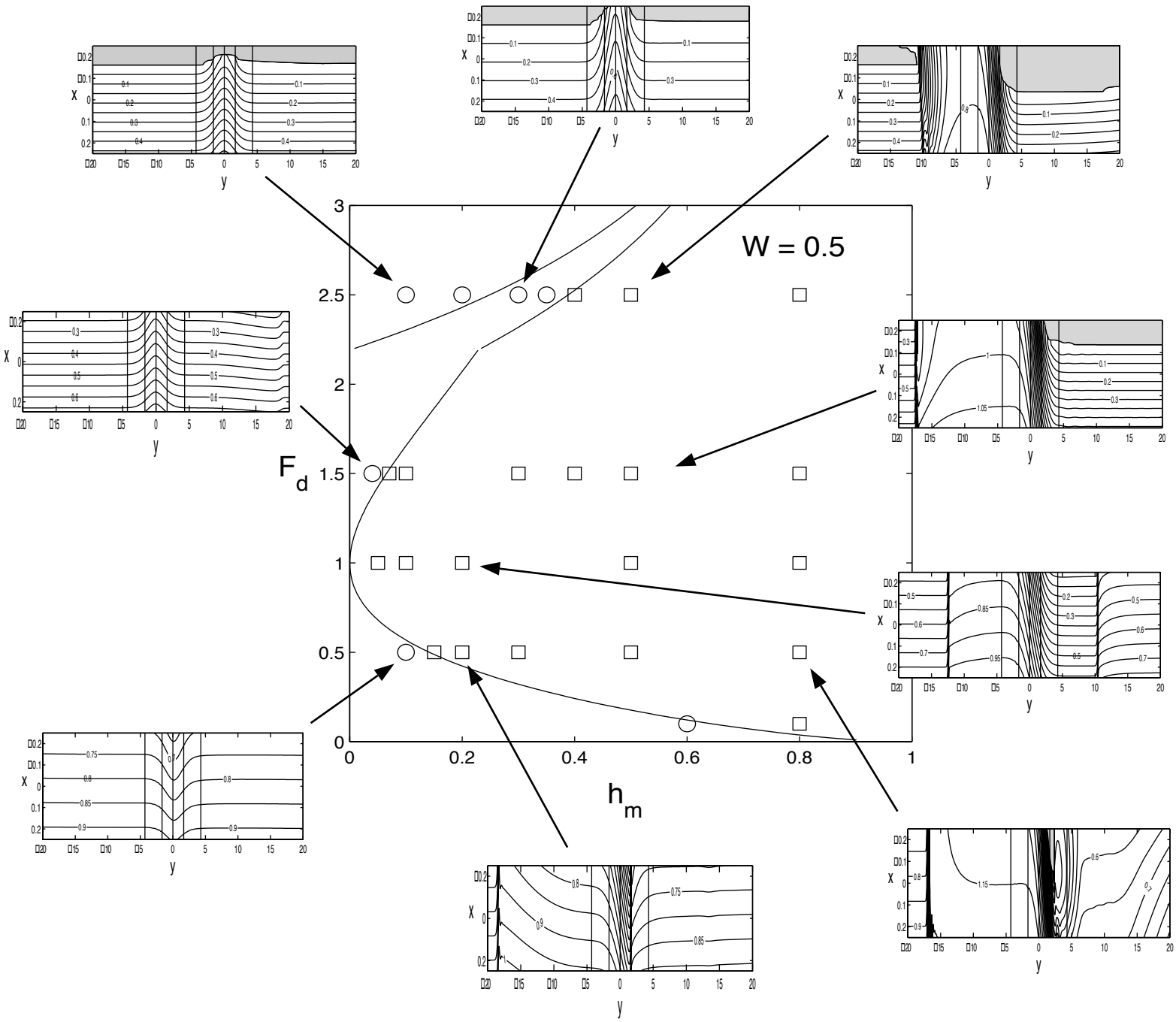

3.4.3

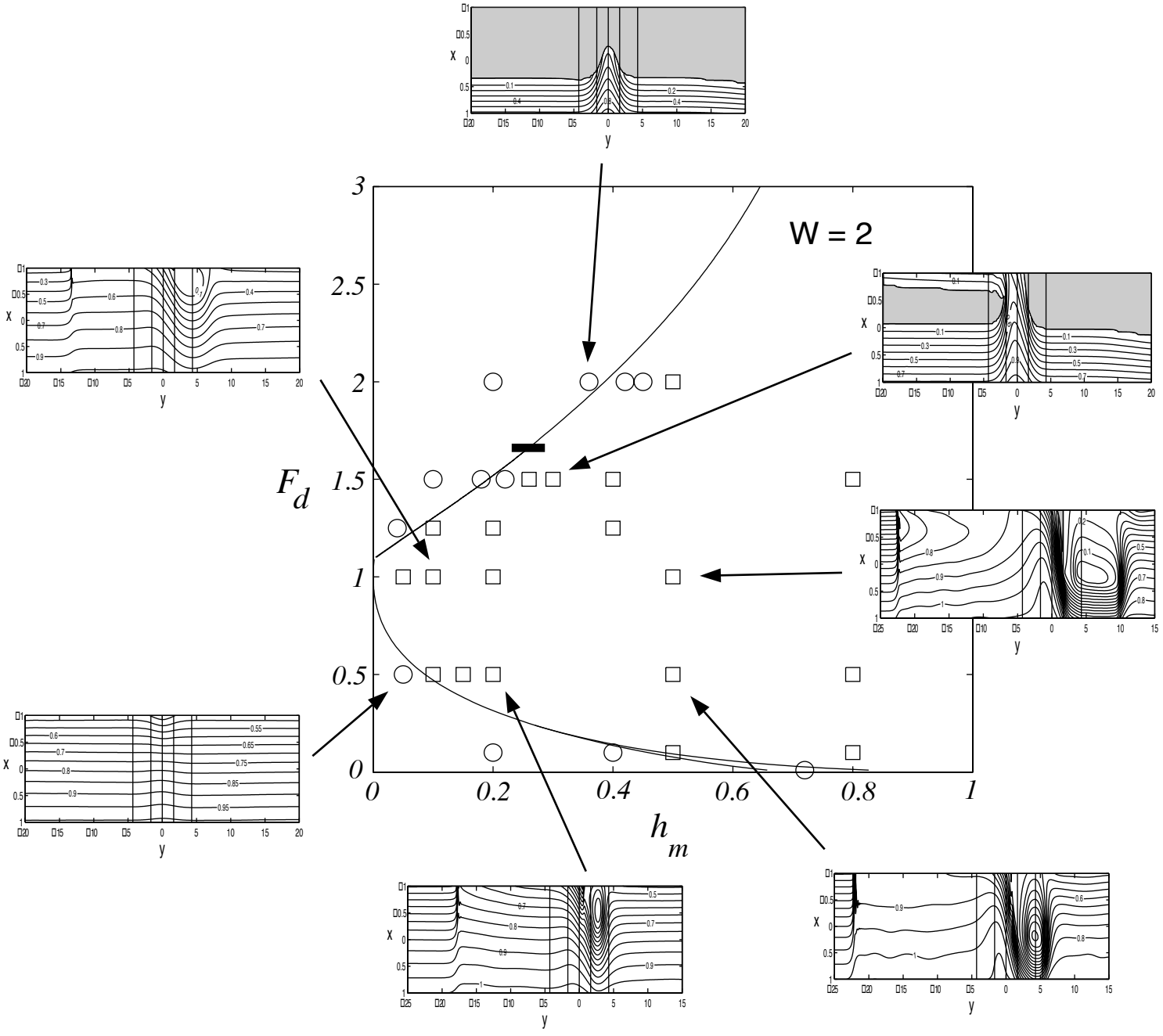

3.4.4

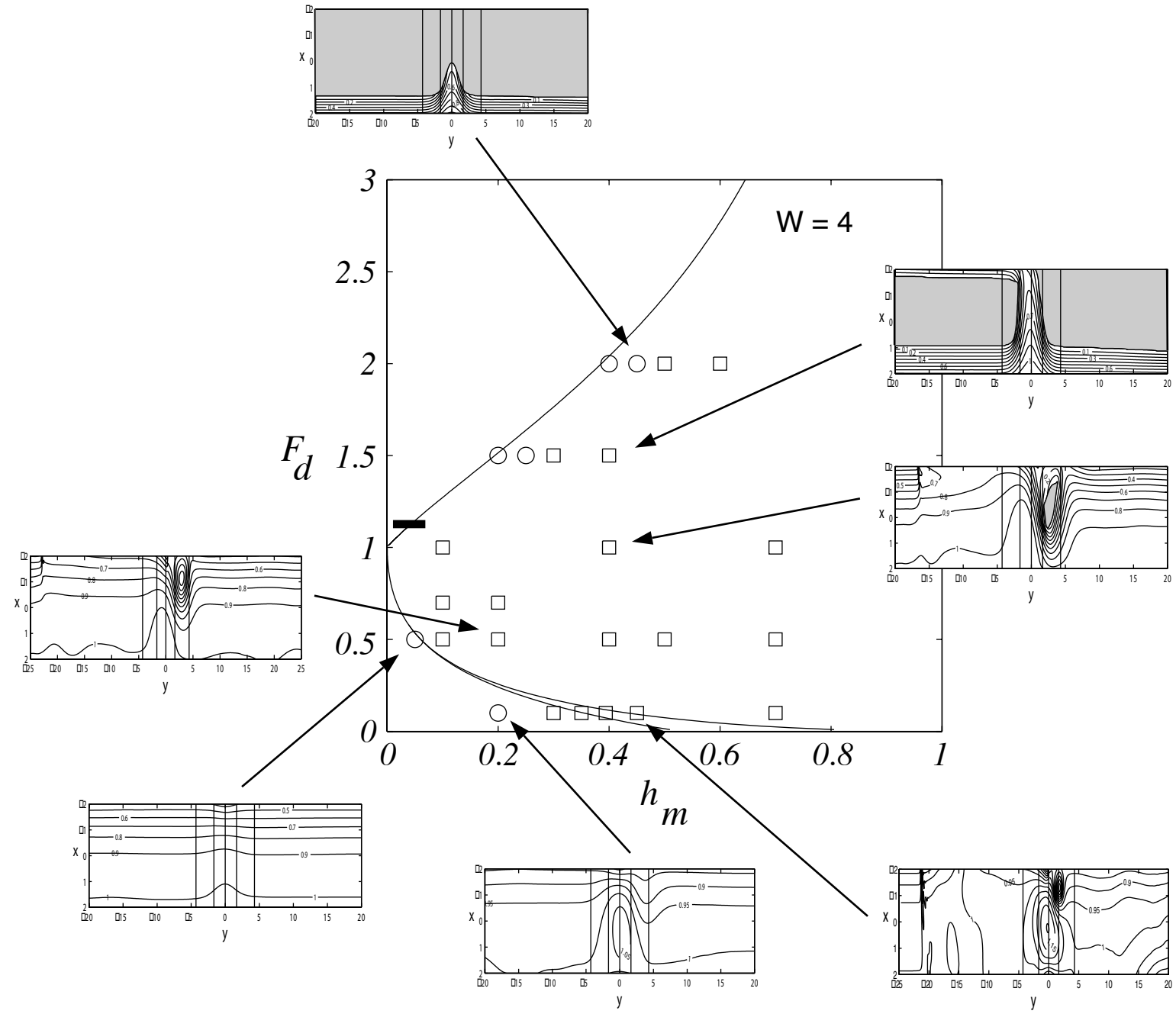
W = 4
F_d
h_m
3
2.5
2
1.5
1
0.5
0
0
0.2
0.4
0.6
0.8
1
x
y

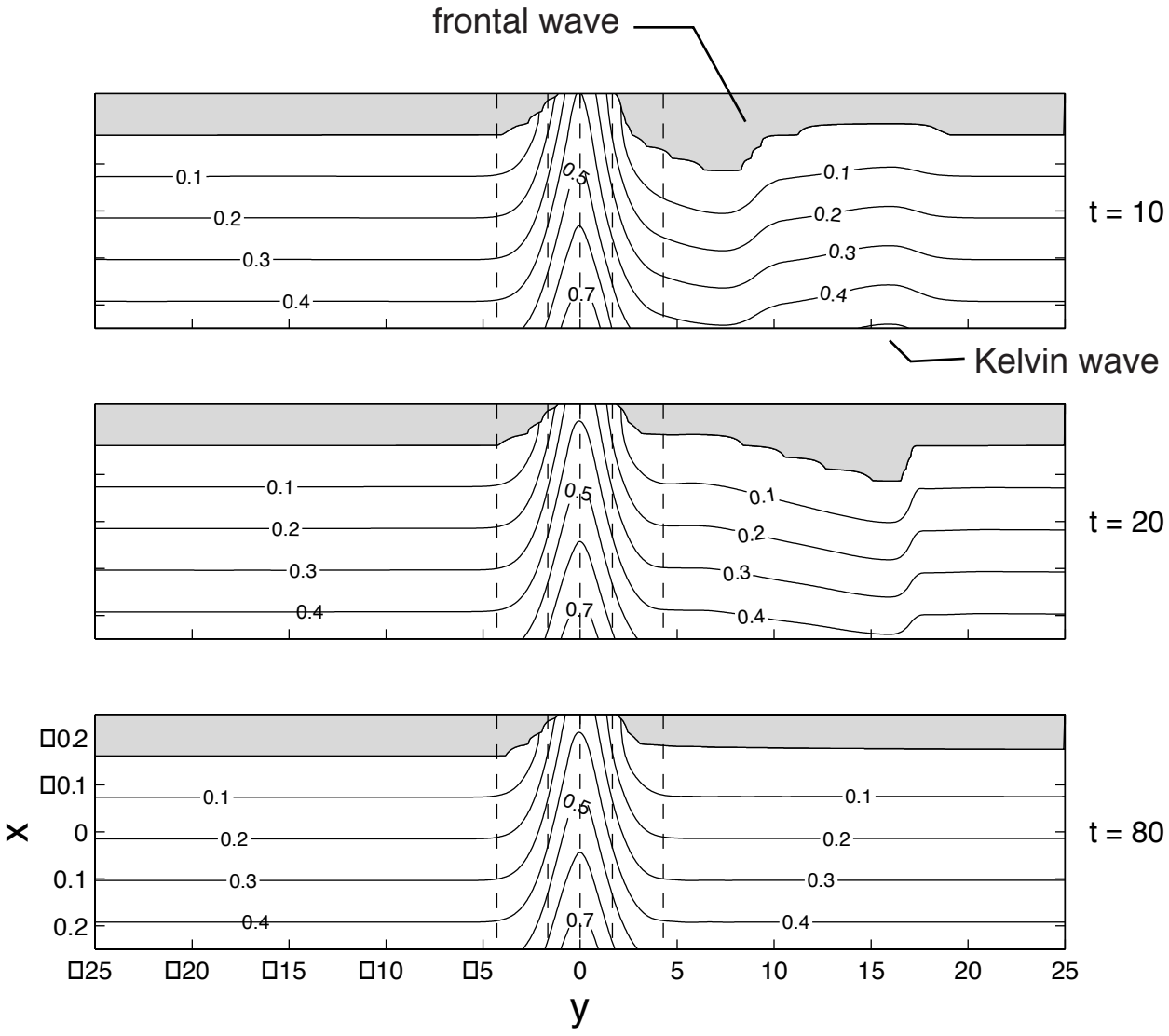
frontal wave
Kelvin wave
t = 10
t = 20
t = 80
0.1
0.2
0.3
0.4
0.5
0.7
x
y
□0.2
□0.1
0
0.1
0.2
□25
□20
□15
□10
□5
0
5
10
15
20
25

Fig. 3.4.6

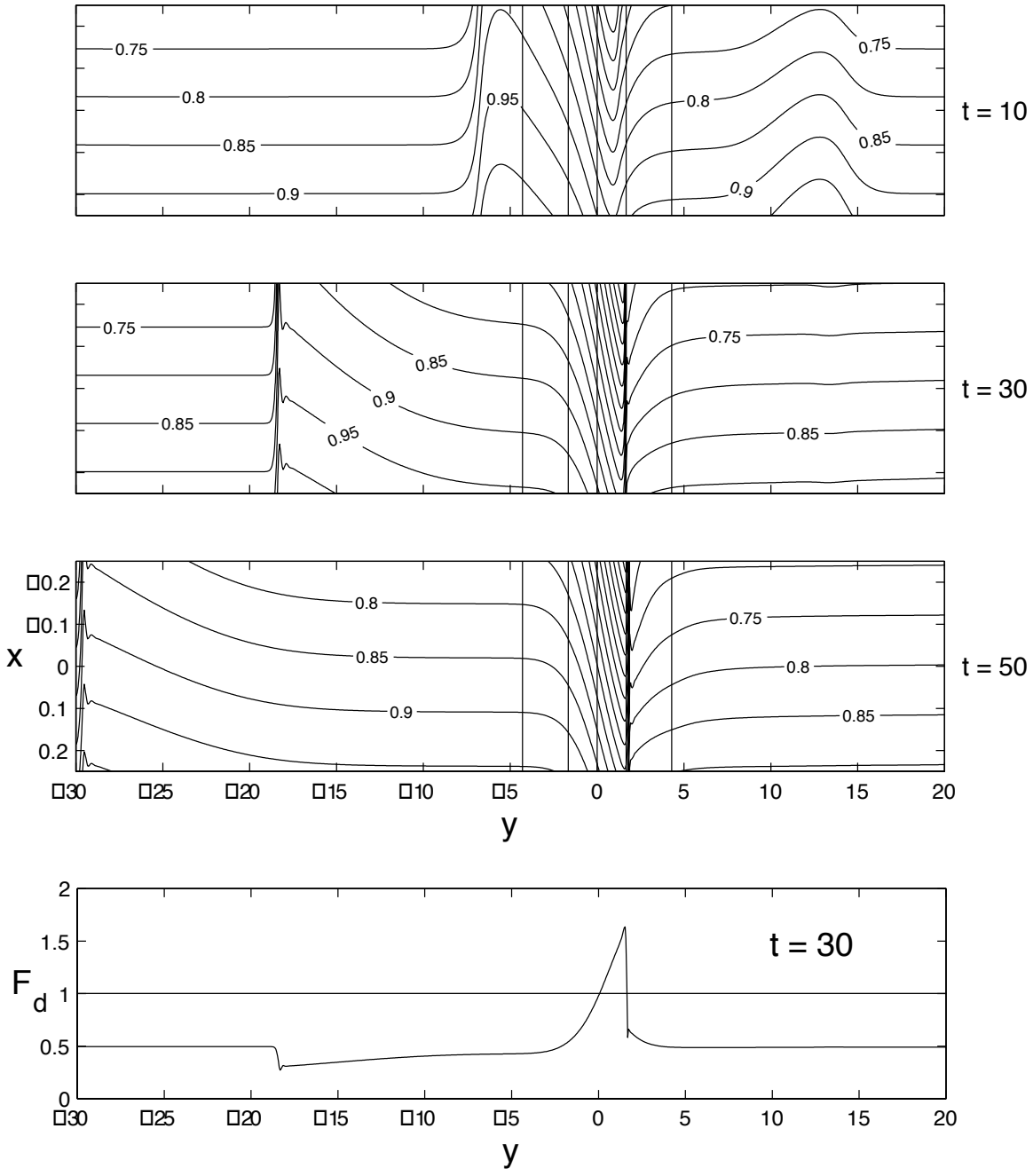

Fig 3.4.7

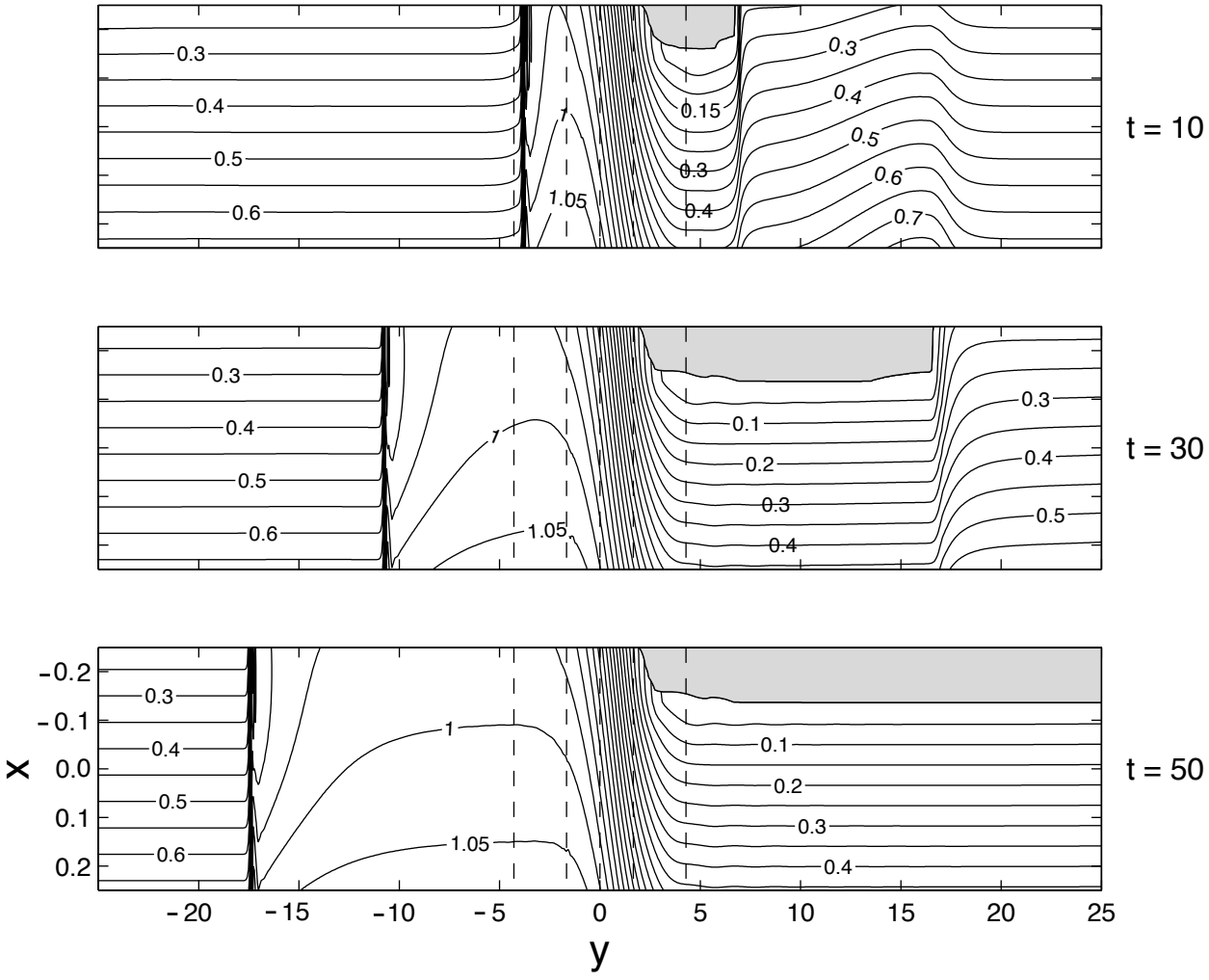
0.3
0.4
0.5
0.6
1
1.05
0.15
0.3
0.4
0.3
0.4
0.5
0.6
0.7
t = 10
0.3
0.4
0.5
0.6
1
1.05
0.1
0.2
0.3
0.4
0.3
0.4
0.5
t = 30
-0.2
-0.1
0.0
0.1
0.2
x
0.3
0.4
0.5
0.6
1
1.05
0.1
0.2
0.3
0.4
t = 50
-20
-15
-10
-5
0
5
10
15
20
25
y

Fig. 3.4.8

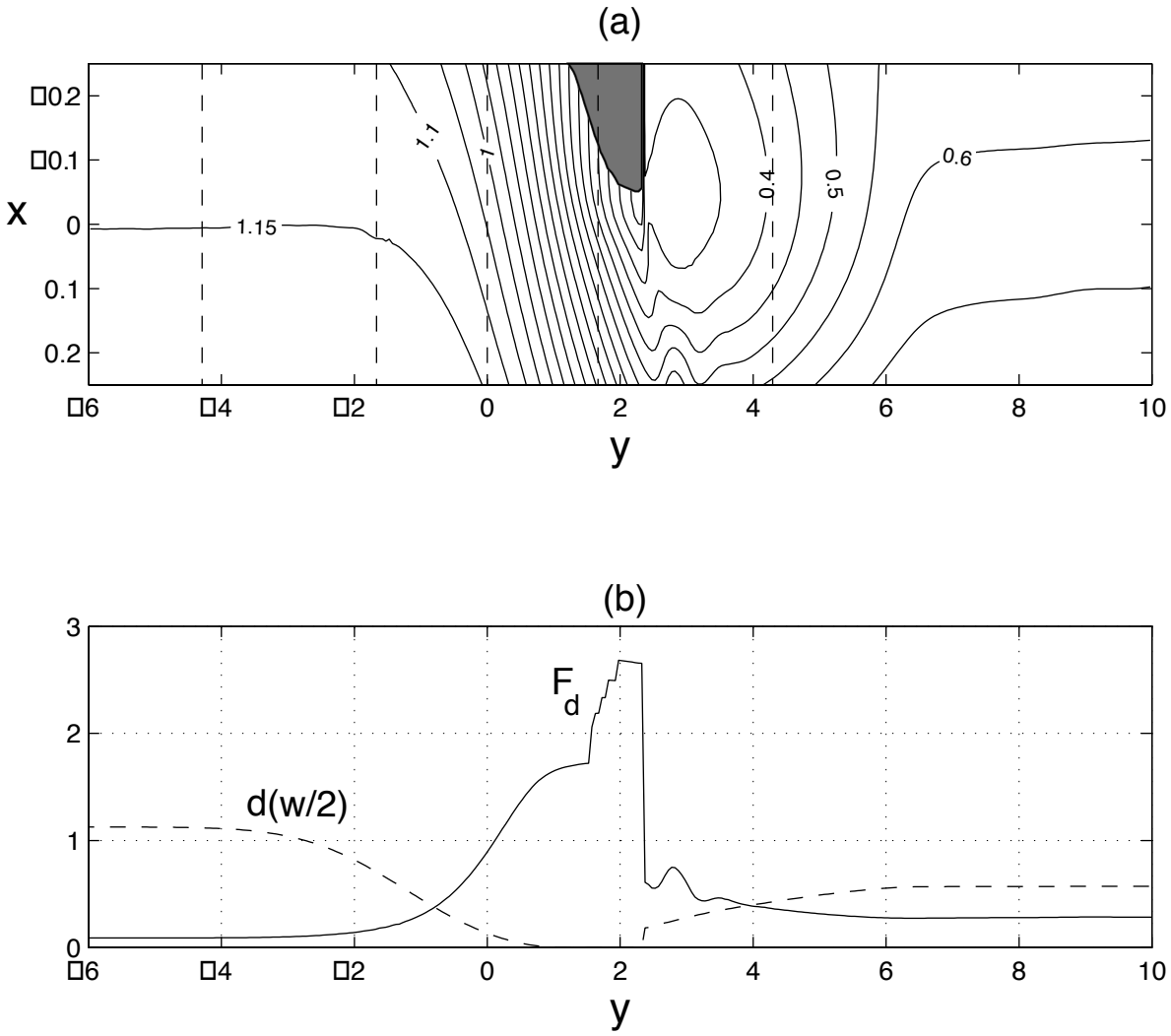

Fig. 3.4.9

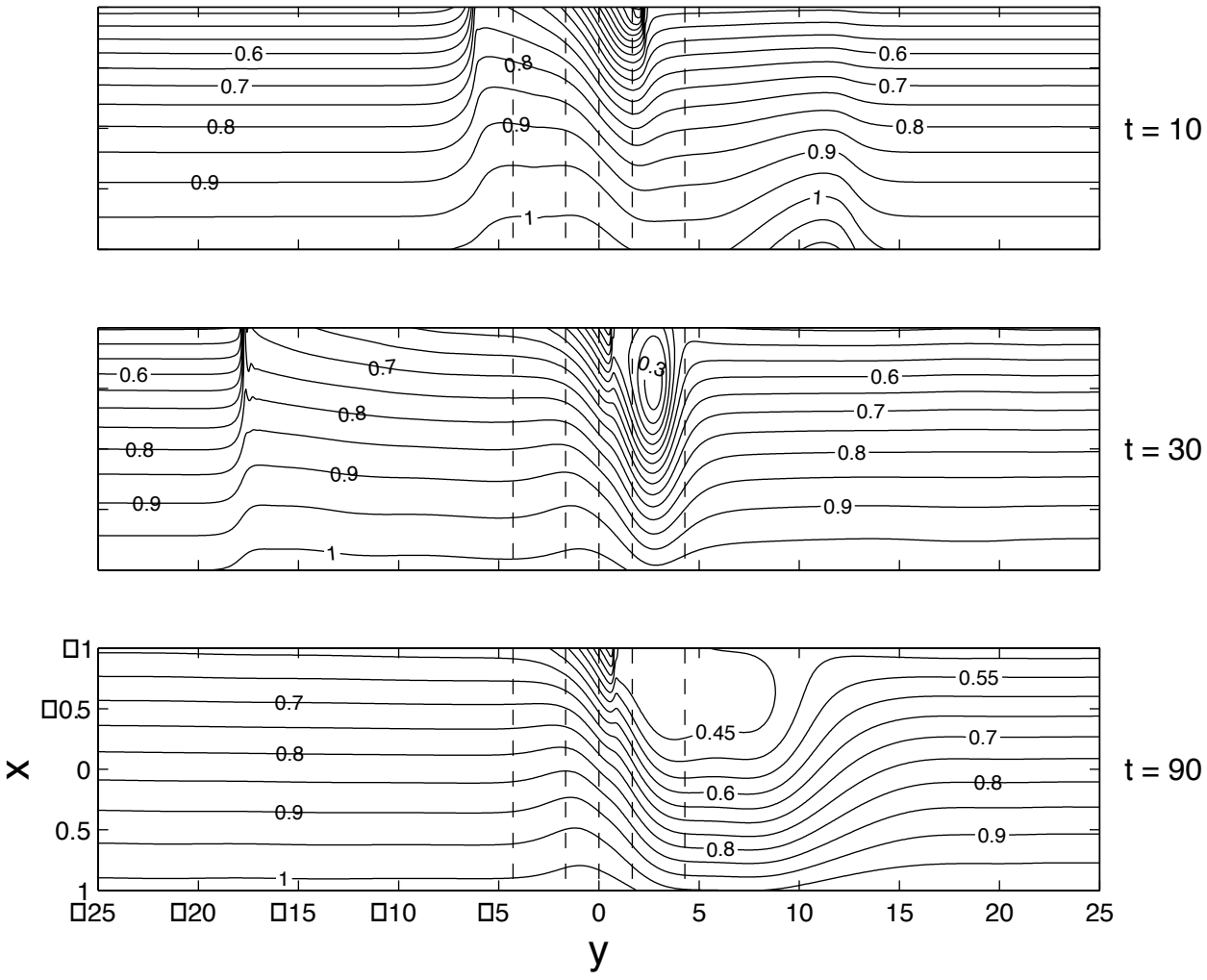
0.6
0.7
0.8
0.9
1
t = 10
0.3
0.55
0.45
t = 30
t = 90
x
y
□1
□0.5
0
0.5
1
□25
□20
□15
□10
□5
5
10
15
20
25

Fig. 3.4.10

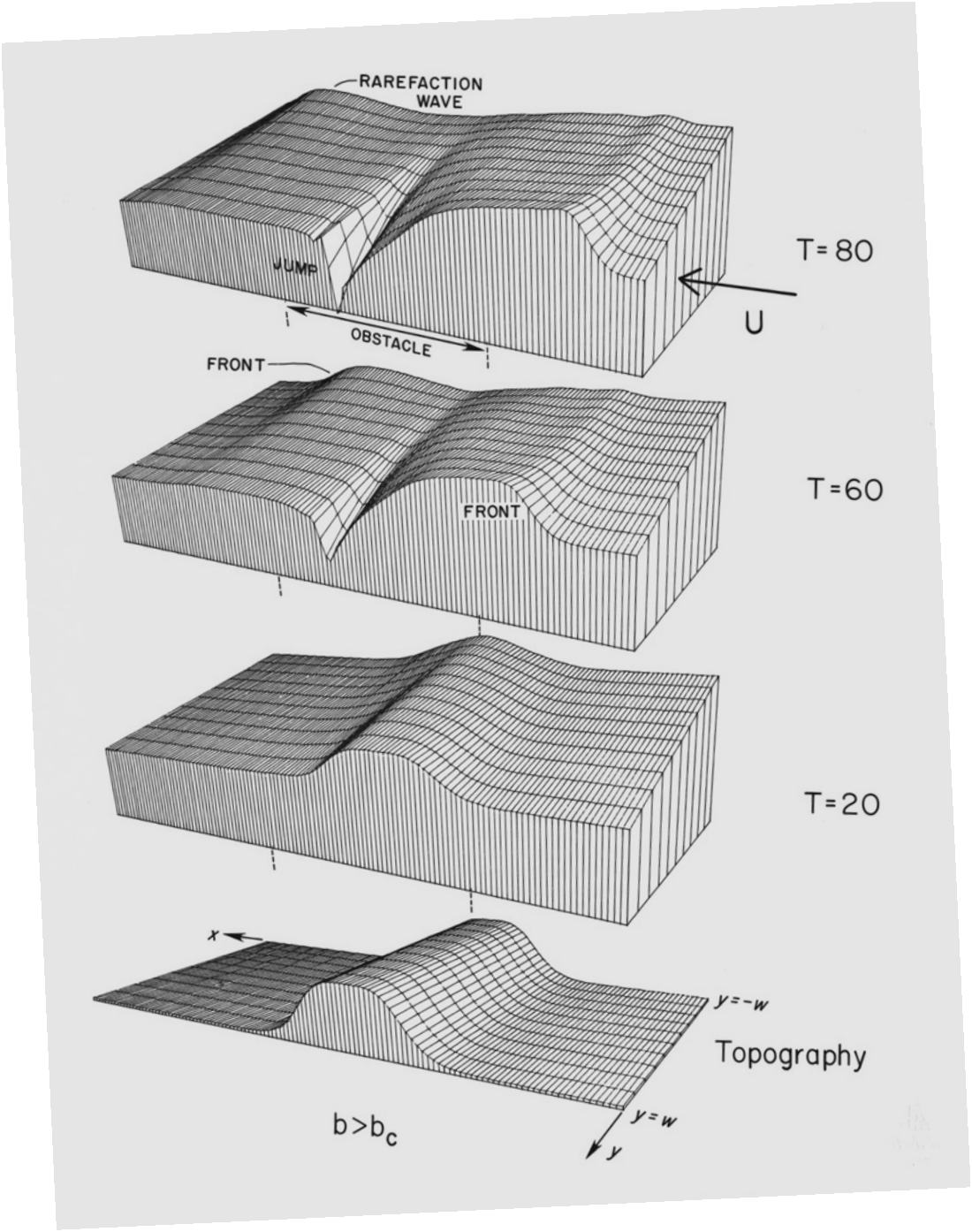

Figure 3.4.11 (low resolution version)

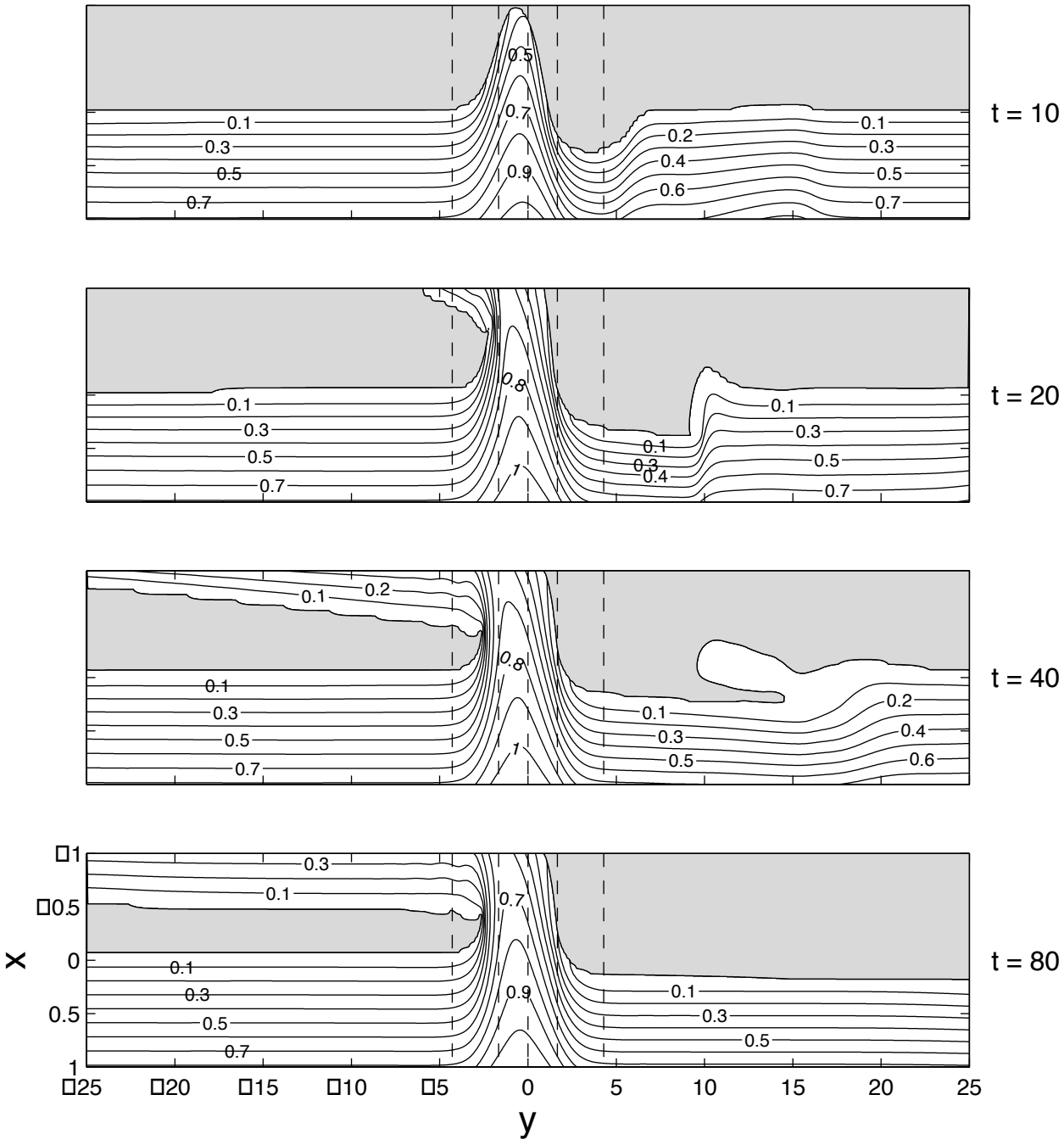

Fig. 3.4.12

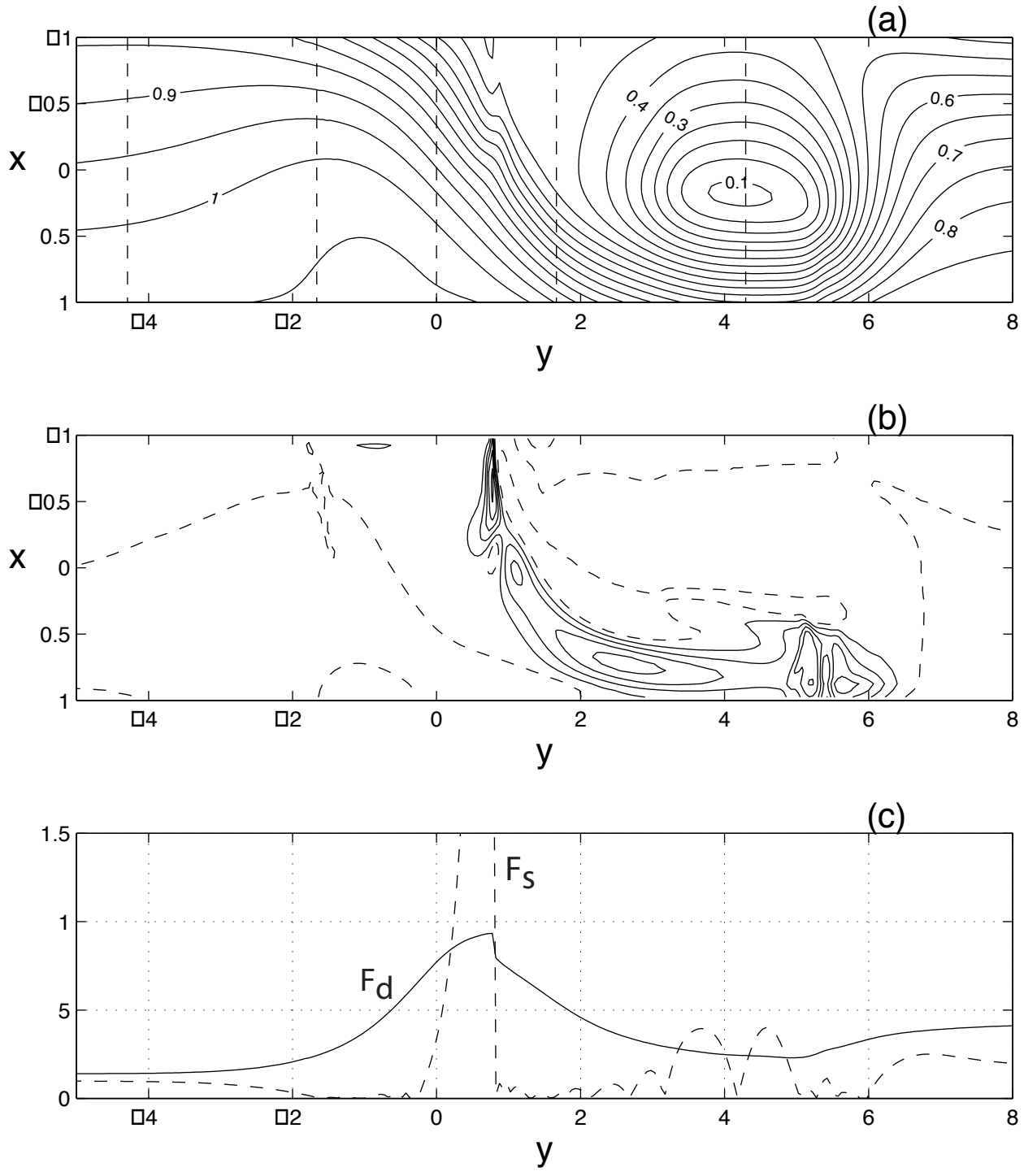

Fig. 3.4.13

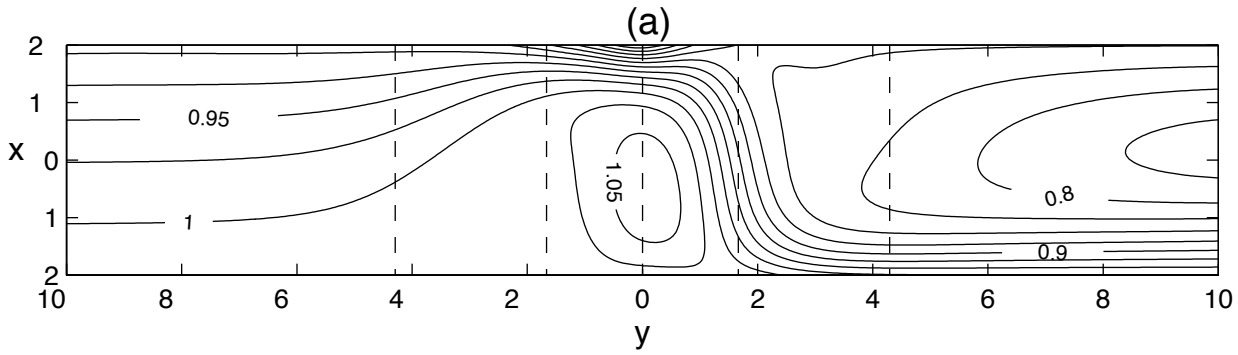

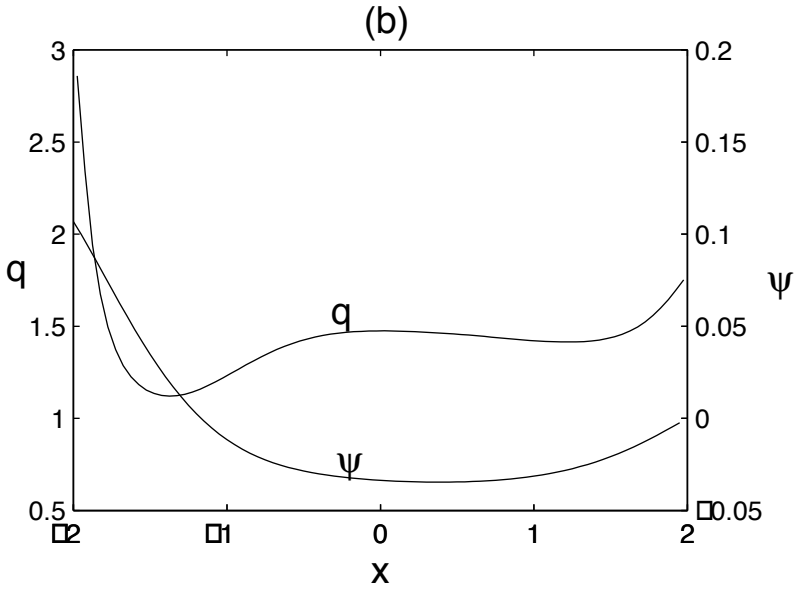

Figure 3.4.14